N-Doping Effects On Electrocatalytic Water Splitting of Non-Noble High-Entropy Alloy Nanoparticles Prepared by Inert Gas Condensation

Xuechun Zhou, Lvyu Zou, He Zhu, Mengyang Yan, Junjie Wang, Si Lan, Shuangqin Chen, Horst Hahn, and Tao Feng**

The unique catalytic activities of high-entropy alloys (HEAs) emerge from the complex interaction among different elements in a single-phase solid solution. As a "green" nanofabrication technique, inert gas condensation (IGC) combined with laser source opens up a highly efficient avenue to develop HEA nanoparticles (NPs) for catalysis and energy storage. In this work, the novel N-doped non-noble HEA NPs are designed and successfully prepared by IGC. The N-doping effects of HEA NPs on oxygen evolution reaction (OER) and hydrogen evolution reaction (HER) are systematically investigated. The results show that N-doping is conducive to improving the OER, but unfavorable for HER activity. The FeCoNiCrN NPs achieve an overpotential of 269.7 mV for OER at a current density of 10 mA cm^{-2} in 1.0 M KOH solution, which is among the best reported values for non-noble HEA catalysts. The effects of the differences in electronegativity, ionization energy and electron affinity energy among mixed elements in N-doped HEAs are discussed as inducing electron transfer efficiency. Combined with X-ray photoelectron spectroscopy and the extended X-ray absorption fine structure analysis, an element-design strategy in N-doped HEAs electrocatalysts is proposed to improve the intrinsic activity and ameliorate water splitting performance.

1. Introduction

High-entropy alloys (HEAs) with near-equiatomic proportions have received considerable attention in terms of synthesis and application, especially in catalysis and energy storage owing to their unique atomic structure including the cocktail effect, lattice distortion effect, slow diffusion effect and high entropy effect.[1–3] Multi-element interactions can result in a divergence of the properties and states of the center atoms. Moreover, the nanostructures of HEAs boost.[4] However, it is still a focus task to integrate multiple elements into HEAs at the nanoscale. Inert gas condensation (IGC) with laser source,[5] as a "green" distinctive physical route for scalable nanofabrication, could hew out a highly efficient avenue to tune the atomic structure of HEA nanoparticles (NPs) including heteroatom doping for various applications. The ultrafast laser ablation and cooling processes ensure the multiple metallic elements uniformly combining regardless of their thermodynamic solubility,[6] which differentiate from the general synthesis techniques, such as rapid Joule-heating,[7] moving bed pyrolysis,[8] electrosynthesis and so on.[9]

Oxygen evolution reaction (OER) is a crucial half reaction in renewable-energy conversion and storage technologies, while its dilemma of the complicated four-electron transfer and sluggish reaction urgently needs to be broken.[10–12] Moreover, considering the scarcity, high cost and poor durability of RuO_2 and IrO_2 as superior active catalysts for OER, 3d transition metals with low cost and tunable electronic structure have been preferred and extensively studied in recent years.[13,14] Compared with single-element transition metals, multi-element transition metal-based electrocatalysts typically endow more superior activities, as the interatomically electronic interplay can efficiently modulate the electronic configuration of metal sites to reduce the kinetic energy barriers.[15,16] Notably, HEAs as a recently focus in the field of electrocatalysis, their unconventional compositions and infinite elemental combinations offer many possibilities for regulating catalytic performance and overcoming the limitations of conventional binary or ternary alloys.[17] Generally, heteroatom (e.g., N, P, B, and S) doping in compounds has been proven to be an effective method to adjust the adsorption or desorption energy of the reaction intermediates via tuning the interactions between metal atoms and the electronic structure of catalysts.[18–20] Among them, N atoms tend to occupy the vacant positions in the lattice due to its small radius, forming "interstitial compounds".[21] This unique arrangement of atoms is

X. Zhou, L. Zou, H. Zhu, M. Yan, J. Wang, S. Lan, S. Chen, H. Hahn, T. Feng
Herbert Gleiter Institute of Nanoscience
School of Material Science and Engineering
Nanjing Nanjing University of Science and Technology
Nanjing 210094, China
E-mail: lansi@njust.edu.cn; tao.feng@njust.edu.cn
H. Hahn
Institute of Nanotechnology
Karlsruhe Institute of Technology
76021 Karlsruhe, Germany

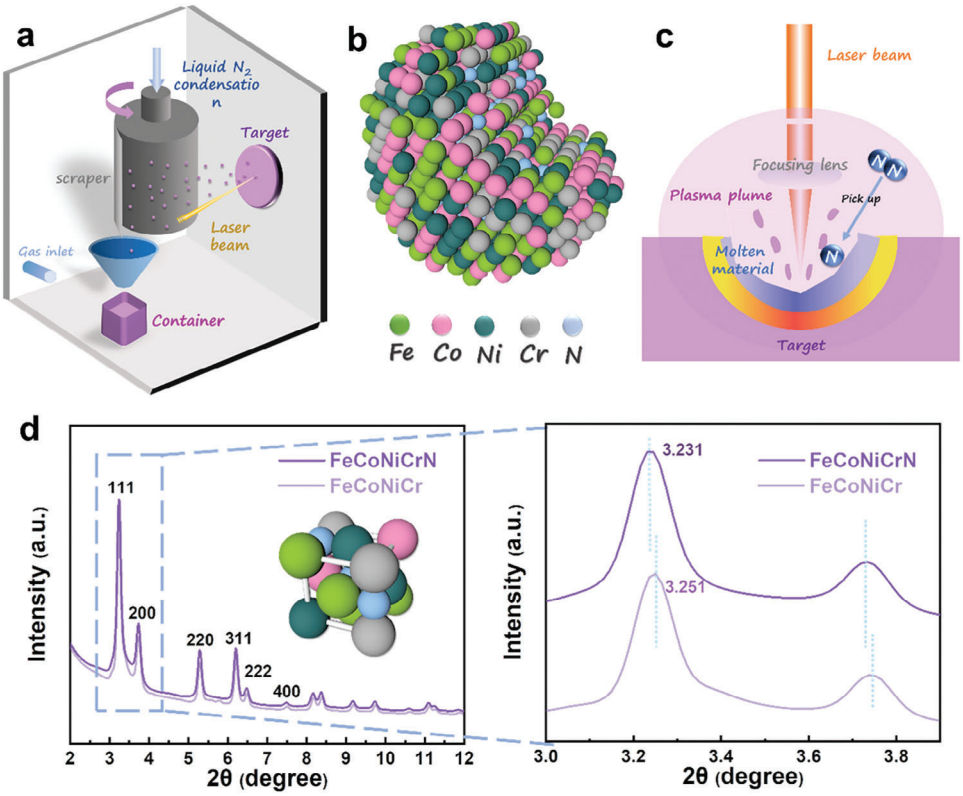

Figure 1. a) Schematic diagram of IGC system and laser preparation of HEA NPs; b) Diagram of FeCoNiCrN NPs; c) Schematic illustration of the in situ doping via IGC system under reactive N_2 atmosphere; and d) Synchrotron high-energy XRD patterns and corresponding partial enlarged view.

endowed with an attractive electric conductivity.[22,23] The introduction of N atoms to transition metals causes lattice expansion and redistribution of the density of states near the Fermi energy level, ameliorating the states density of d-band electron, while the contraction of d-band makes their electronic structure similar to that of precious metals.[24,25] Numerous studies have been devoted to focusing on transition metal nitrides due to their high electric conductivity, good corrosion resistance and high hardness,[26] thus designing N-doped HEAs are expected to be an ideal replacement for precious metals in electrocatalytic applications.

In this work, a facile alloying and unique nanofabrication strategy is reported to successfully synthesize N-doped non-noble HEA NPs via an IGC system. The HEA NPs with uniform elemental distribution are generally formed in a short period of time (picoseconds). The non-noble HEA NPs with 1.93 at. % N-doping exhibit a better OER catalytic performance which could be ascribed to the greater electronegativity of N atom than transition metals, inducing interfacial charge transfer effect. The higher density of activated electrons due to the electronic effects of N-doped HEAs are conducive to improving the OER activity. Interestingly, FeCoNiCrN NPs emerge with better electrocatalytic properties than FeCoNiCrMnN for OER, while FeCoNiCrMn NPs exhibit better HER performance. Thus, the effect of ionization energy and electron affinity energy on electron transfer is also taken into account. Furthermore, based mainly on the electron valence analysis via the extended X-ray absorption fine structure (EXAFS) and X-ray photoelectron spectroscopy (XPS), a reasonable inference on electron transfer in N-doped HEAs electrocatalysts is proposed, which may offer a feasible approach to tune the electrocatalytic intrinsic activity.

2. Results and Discussion

2.1. Characterization

The IGC method is an efficient and green way to introduce interstitial nitrogen into HEAs using N_2 as the nitrogen source while maintaining a single-phase structure. This method addresses the critical challenge commonly encountered in traditional casting techniques, where N_2 easily escapes at high temperature.[27] The scheme of preparation is illustrated in **Figure** 1a–c, with the specific methods in the experimental section. From the results of EDS, the content of N doping is ≈2–7 at. %, which confirms the feasibility of the scheme (Table S1, Supporting Information). The synchrotron high-energy XRD patterns without the presence of impurity peaks imply that both undoped and N-doped FeCoNiCr and FeCoNiCrMn HEA NPs maintain a single-phase face-centered cubic (FCC) structure, as shown in Figure 1d and Figure S1 (Supporting Information), respectively. For FCC structure, there are tetrahedral gap and octahedral gap for N atoms to diffuse, and the size of the octahedral gap is larger than that of the tetrahedral gap, and the N atoms preferentially enter the octahedral gap during diffusion. The diffraction peaks corresponding to (1 1 1), (2 0 0), (2 2 0), and (3 1 1) planes of the FCC structure are evident in the as-synthesized samples.

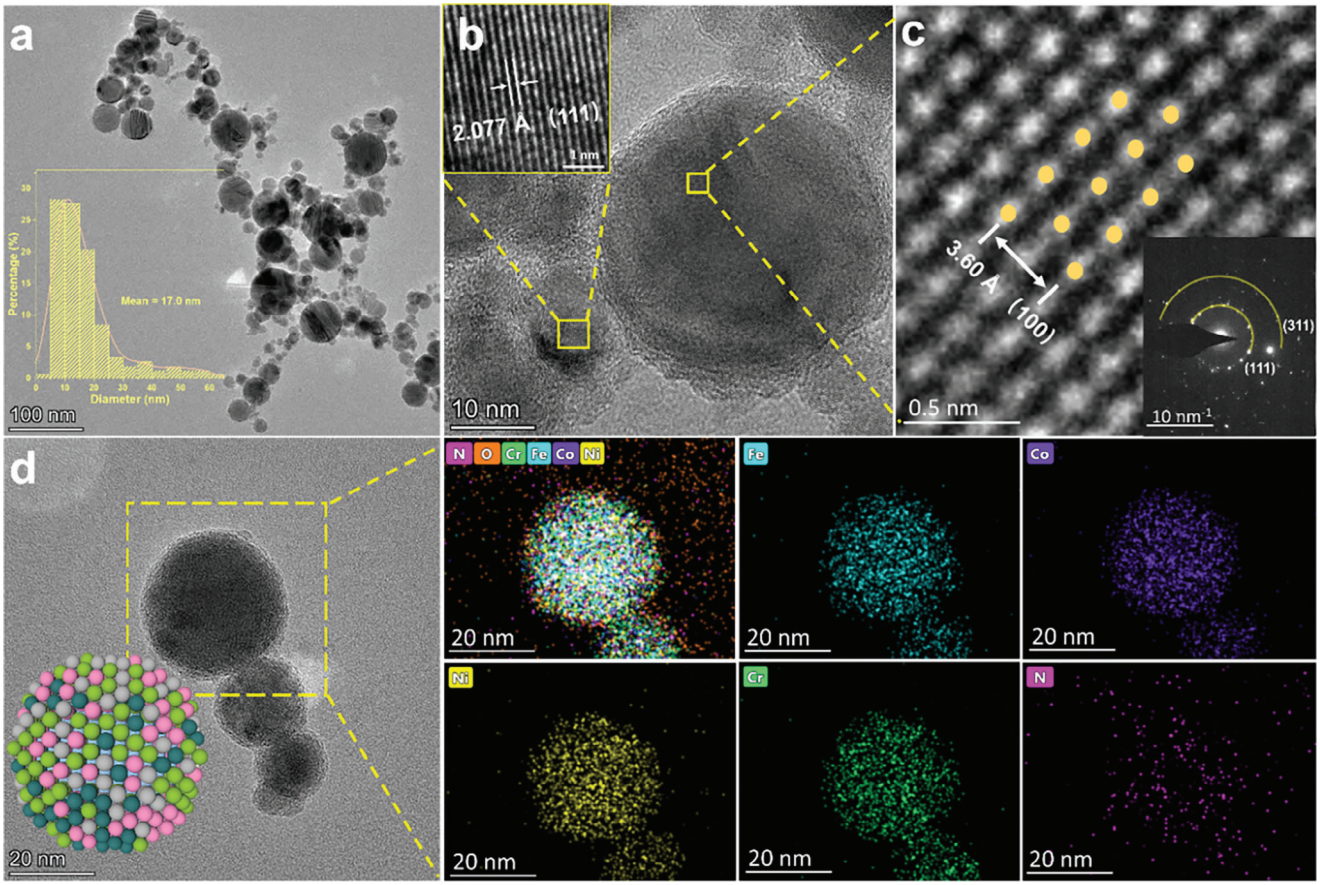

Figure 2. a—c) TEM and c HRTEM images of the FeCoNiCrN NPs sample; Particle size distribution chart (inset in a); SAED of FeCoNiCrN NPs (inset in c); d) EDS mappings of FeCoNiCrN NPs.

With the implementation of the high entropy concept, multiple elements can be incorporated into a single-phase structure, thereby enabling various catalytic centers in a single compound. The XRD peaks shift to lower angles after N doping (3.251 to 3.231), corresponding to the interplanar spacings of (1 1 1) expand from 2.064 Å for FeCoNiCr to 2.075 Å for FeCoNiCrN according to the refinement of XRD data, representing ≈0.53% tensile strain.[28] The lattice parameters are calculated as 3.5946 Å for FeCoNiCrN and 3.5823 Å for FeCoNiCr, which also confirms that the nitrogen as a gap atom is dissolved into the FCC matrix.[29]

As shown in **Figure 2**a, the average size of FeCoNiCrN NPs is ≈17.0 nm, whereas that of FeCoNiCr NPs is slightly larger, ≈19.8 nm (Figure S2b, Supporting Information). A similar phenomenon has been observed in FeCoNiCrMnN (Figure S3, Supporting Information). For N-doped HEAs, the increased solubility raised the composition of nitrogen in the melting zones. Nitrogen enrichment may remarkably refine grain size during solidification, as literature reported.[30] In addition, during solidification, the faster the cooling rate, the more nucleation sites there are and the smaller the grain size will be. The large amount of undercooling achieved by the IGC technique is due to the high cooling rate which originates from the collision with gas atoms as well as the extremely large temperature gap between vapor region and the liquid-nitrogen filled cold finger.[6] The HEA NPs formation via IGC is actually a process far from the equilibrium state instead of relying on their thermodynamic solubility. From Figure 2b,c, the HRTEM image and corresponding selected area electron diffraction (SAED) pattern of FeCoNiCrN reveal the consistent crystal phase with the XRD pattern. The crystal plane spacing of lattice stripes (Figure S4, Supporting Information) suggests a larger lattice distance of FeCoNiCrN compared with FeCoNiCr (1 1 1) spacing of 2.065 Å, which represents ≈0.58% tensile strain and approaches to the XRD refinement results. Therefore, the presence of N within the FeCoNiCrN NPs can lead to the distortions of FeCoNiCr lattice, thus resulting in the tensile strain effect. The HRTEM image in Figure 2c was captured along $[0\ 1\ 1]_{FCC}$ axis, where the (1 0 0) interplanar spacing was determined to be 3.60 Å. The clear crystal lattices suggest the high crystallization degree of HEA NPs. Each metal element uniformly and randomly distributes throughout the HEA NPs by EDS mapping (Figure 2d; Figure S5, Supporting Information). The Fe, Co, Ni, Cr, and Mn content are similar and the N element content is less, which also confirms the successful N doping. The formation of homogeneous elemental distribution is attributed to the lattice distortion and low atomic diffusivity upon mixing during the rapid cooling process, effectively preventing NPs from phase separation.[31,32] In addition, the sluggish diffusion effect of HEAs can suppress the coarsening of nanostructured HEA catalysts.

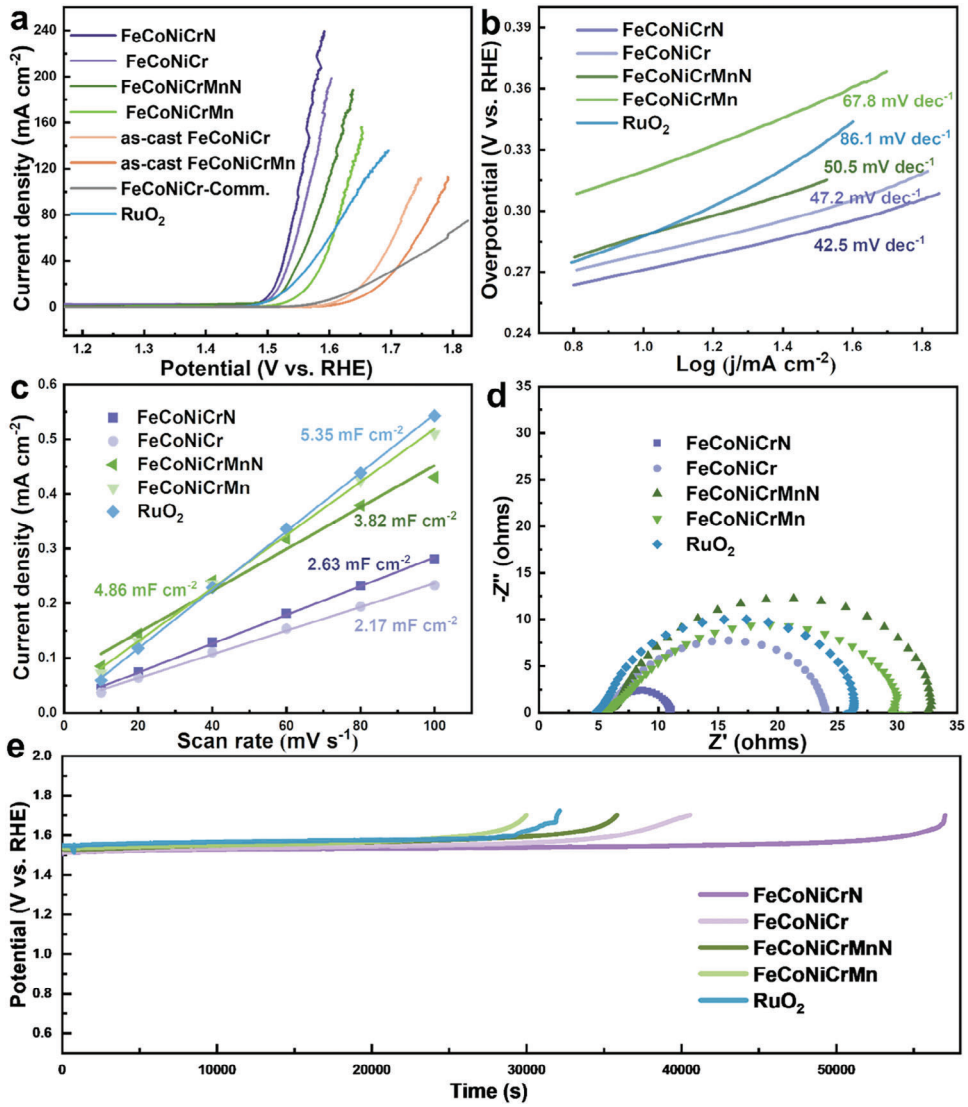

Figure 3. a) IR-corrected polarization curves of the different electrocatalysts for OER in 1.0 M KOH solution at room temperature; b) The corresponding Tafel plots of the different electrocatalysts; c) Current density differences plotted against scan rate of the different electrocatalysts; d) The corresponding EIS spectra; e) Chronopotentiometry curve obtained with the different electrocatalysts at a constant current density of 10 mA cm^{-2}.

2.2. Electrochemical Evaluation

The OER performance of IGC-prepared HEA NPs was tested in 1.0 M KOH solution using a typical three-electrode system.[33] Quaternary and quinary as-casted bulk HEAs were also employed for comparison. In order to prove that the carbon black only functions as a supporter and current collector during the electrochemical test, carbon black with the same concentration was checked as the control group, which had almost no electrochemical activity as shown in Figure S6 (Supporting Information). **Figure 3a** shows the LSV plots of various electrode materials, which can visually reflect the oxygen evolution ability. Among them, FeCoNiCrN exhibits the lowest overpotential of 269.7 mV at a current density of 10 mA cm^{-2}, which is even lower than the commercial RuO_2 (287.8 mV) and much lower than that of most reported non-noble metal catalysts.[34] Especially, it has the best OER performance at high current densities. In addition to the overpotential, the Tafel slope is another important parameter for evaluating the electrocatalytic performance, as well as reflects the energy conversion efficiency of the catalyst. Generally, a smaller Tafel slope within a reasonable range infers faster kinetics based on a similar mechanism. From Figure 3b, the Tafel slope of FeCoNiCrN, FeCoNiCr, FeCoNiCrMnN, and FeCoNiCrMn, derive from the LSV curve, are 42.5, 47.2, 50.5, and 67.8 mV dec^{-1}, respectively, which are all smaller than that of commercial RuO_2 (86.1 mV dec^{-1}), indicating faster OER kinetics and catalytic rate. The unique catalytic activities of HEAs emerge from the complex interaction among different elements in a single-phase solid solution. In addition, Tafel slope within the range of 30 – 80 mV dec^{-1} is more conducive to the surface interstitial formation of intermediates on the catalyst surface during OER.[35] The smaller Tafel slope may be explained by the increased adsorption capacity of the

electrocatalyst for OH^-. In brief, the Tafel analysis supports the superior activity of HEA NPs prepared by the IGC system for the OER application, which is also attributed to the more available surface-active sites due to the nanometer size. As expected, N-doping, as an effective means, can improve the OER performance. In order to further assess the OER catalytic activity, the electrochemical activity specific surface areas (ECSA) of catalysts were investigated by the double-layer capacitance (C_{dl}), which measure by CV curves at various scan rates in the non-Faraday region.[36] The ECSA values of FeCoNiCr, FeCoNiCrN, FeCoNiCrMn, FeCoNiCrMnN and Ru_2O were calculated to be 10.6, 12.9, 23.8, 18.7 and 26.2 cm^2, respectively. An interesting phenomenon is shown in Figure 3c, the linear slope of FeCoNiCrMn(N) is larger than FeCoNiCr(N), indicating a larger electrochemically active area and a higher intrinsic OER activity. It seems contrary to the actual electrochemical properties. In general, the addition of a fifth element as substitutional element may modify the electronic structures of the HEA, thereby affecting the catalytic activities. Nevertheless, it is necessary to consider not only the inherent synergetic effect in the combination of multiple active metals but also the electronegativity and oxidation state of the added metal for improving catalytic performance.[37] The resistance located in the high frequency region reflects the ohmic resistance (R_s), meanwhile the charge transfer resistances (R_{ct}) are related to the arc radius of the Nyquist plot in Figure 3d. The FeCoNiCrN exhibits a prominent interfacial charge transfer resistance of ≈5.7 Ω as compared to that of other electrocatalysts, which is consistent with their OER activities and signifies the obviously greater reaction kinetics, attributed to the improved charge-transfer rate, faster reactant adsorption, and conversion of intermediates.[38] The catalytic stability as an important property to assess an outstanding catalyst is shown in Figure 3e. The long-term electrolysis was investigated by chronopotentiometry measurement with a current density of 10 mA cm^{-2}. It is clear to see that FeCoNiCrN provides excellent stability performance with overpotential slight amplification for 50 000 s in alkaline conditions at a static current density of 10 mA cm^{-2}. Moreover, the FeCoNiCrN NPs present negligible structural and compositional change after OER stability testing (Figure S7, Supporting Information). The elemental maps of the used HEA NPs further reveal that each element is uniformly distributed without phase separation, which provides dispersed active sites. Intuitively enough, the FeCoNiCrN NPs have the most outstanding OER performance among these electrocatalysts with the lowest overpotential (Figure S8a, Supporting Information) and best stability. The precursors of HEA NPs, i.e., as-cast alloys, exhibit very poor catalytic performance with over 400 mV of overpotential at a current density of 10 mA cm^{-2}. Moreover, the commercial FeCoNiCr (FeCoNiCr-Comm.) is examined with 389.4 mV at 10 mA cm^{-2}, and even exhibits the awful OER performance at a high current density, reflecting the high activity of nanomaterials prepared by IGC system again. To further illustrate the stability of FeCoNiCrN/C at high currents, 1000 times CV and CP measurement at 100 mA cm^{-2} for OER test are carried out (Figure S9, Supporting Information), which still exhibit better durability.

Furthermore, the HER performance of IGC-prepared HEA NPs was also examined. As shown in **Figure** 4a, FeCoNiCr(Mn) NPs emerge with better electrocatalytic properties than the corresponding N-doped FeCoNiCr(Mn) for HER, which indicates that N-doping in HEA NPs is not always positive on electrocatalytic water splitting. The low electron affinity and high ionization energy (14.5341 eV) of N element induce the resistance to Lewis acid/base, a large energy gap between the highest occupied molecular orbital and the lowest unoccupied molecular orbital,[39] as well as the small atomic radius and high inter-electron repulsion, makes it difficult to gain electrons, which is unfavorable for electron transfer during an electron-absorbing process for HER. Interestingly, FeCoNiCrMn HEA NPs exhibit dramatic HER activity with a low overpotential of 161.8 mV at 10 mA cm^{-2} in the 1.0 M KOH (Figure S8b, Supporting Information). A strong relationship with the electronegativity of the fifth metal in HEA is necessarily focused on. Apart from that, as a function of the hydrogen adsorption strength, the volcano trend about the catalytic activity also needs to be considered due to the difference in atomic configurations involved in changing the adsorption energy.[40,41] The addition of Mn element can optimize the electronic configuration of the catalyst and reduce the free energy of hydrogen adsorption, thus improving the inherent HER activity of the catalyst.[33] Nevertheless, the negative impact of N doping on HER is even greater than the benefits of Mn addition in Figure 4a. FeCoNiCrMn is more prone to doping with N due to the more affinity of N for Mn element and the more negative enthalpy of mixing between them. The similar results can be seen in Table S1 that the N content of FeCoNiCrMnN (6.85 at. %) increased three-fold than that of FeCoNiCrN (1.93 at. %). It can be seen that the lowest Tafel slope (≈117.5 mV dec^{-1}) and the largest ECSA of FeCoNiCrMn NPs indicate the faster kinetics, and the extremely outstanding electrochemically active area (≈10.75 mF cm^{-2}) far beyond other electrocatalysts (≈1 mF cm^{-2}) under the alkaline condition (Figure 4), which is in accordance with the HER activity. In addition, the respective exchange current density values are provided in Figure 4b, FeCoNiCrMn NPs show higher intrinsic activity except Pt/C. The EIS patterns also show that FeCoNiCrMn NPs possess a significantly smaller charge-transfer impedance (R_{ct} = 5.10 Ω) than those of FeCoNiCrN (13.11 Ω), FeCoNiCr (14.03 Ω), and FeCoNiCrMnN (79.36 Ω). It implies that the conductivity of electrons on the surface of FeCoNiCrMn NPs is more suitable for alkaline conditions, and accelerate the electron transport across the catalysts. In addition, the stability test of FeCoNiCrMn NPs was conducted in an Amperometry mode (Figure S10, Supporting Information) and the potential require to maintain the overpotential of 162 mV, which exhibits a slight decline in current density. The results of 1000 times CV and CP measurement at 100 mA cm^{-2} for HER test are further illustrate the good stability of FeCoNiCrMn/C within 15 h (Figure S11, Supporting Information). From the above discussion, FeCoNiCrMn and FeCoNiCrN are taken as the cathode and anode respectively, forming the FeCoNiCrMn//FeCoNiCrN couple, for overall water splitting in 1.0 M KOH, as shown in Figure S12 (Supporting Information). The cell voltage required to achieve a current density of 10 mA cm^{-2} is 1.735 V, higher than the sum of overpotentials of the HER, 0.1618 V, and the OER, 0.2697 V (1.23 + 0.1618 + 0.2697 = 1.66 V), which is mainly attributed to the slightly unstable FeCoNiCrMn electrode. The long-term stability tests for full-cell (FeCoNiCrMn//FeCoNiCrN) at 10 mA cm^{-2} is further investigated in Figure S13 (Supporting Information), and the voltage rises slightly after continuous operation of 35 000 s.

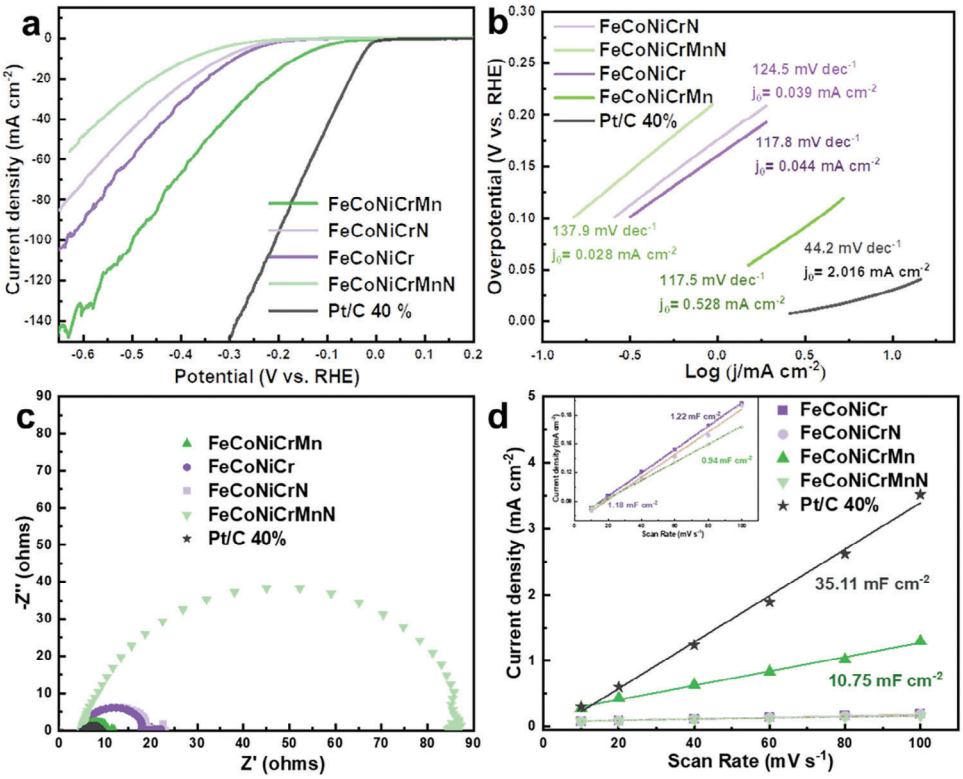

Figure 4. a) IR-corrected polarization curves of the different electrocatalysts for HER in 1.0 M KOH solution at room temperature; b) The corresponding Tafel plots of the different electrocatalysts; c) The corresponding EIS spectra; d) Current density differences plotted against scan rate of the different electrocatalysts.

2.3. Electron Valence Analysis

Multiple processes exist during OER with single-electron transfer in each step, and thus the energy barriers accumulate at each individual step rendering the OER kinetics sluggish causing a high overpotential.[40] Tuning the catalyst electronic structures, as one of the effective strategies to optimize the intrinsic activity of the catalyst for fast electron transfer, is focused on discussion. The surface chemical compositions and valence states of FeCoNiCrN and FeCoNiCr were employed to further investigate by XPS analysis as shown in **Figure 5**. Both samples were etched with argon ions to remove surface oxides as much as possible before XPS measurement due to the easy oxidation of metal powder samples in air. It can be seen that N element is successfully doped into the catalyst, and the Fe 2p, Co 2p, Ni 2p, Cr 2p XPS spectrum of FeCoNiCrN and FeCoNiCr present similar valence state peaks. Notably, an obvious negative shift of FeCoNiCrN to lower binding energy can be observed in the Cr 2p spectrum. Compared with that of FeCoNiCr, the peak shifts of Fe 2p, Co 2p, and Ni 2p are inconspicuous but all of them show a negative shift trend, indicating the electron transfer on surface Fe, Co, Ni, and Cr after N doping. Based on previous literature, the free energies of Co, Fe and Ni nitride formation are positive while Cr has large negative free energies for nitride formation, indicating the more affinity of N for Cr element.[31] Besides, due to the smaller electronegativity of Cr (1.66) compared with that of Ni (1.91), Co (1.88) and Fe (1.8), the electrons near the Cr atom are more easily attracted to the larger electronegativity of N (3.04). This phenomenon is attributed to the possibly existing interfacial charge transfer effect upon doping. The electronegativity of Mn is smaller at 1.55 and yet exhibits poor OER performance which even more consider that Mn possesses a greater ionization energy (7.434 eV) compared to Cr (6.7665 eV). Owing to the electron-donating processes of OER reaction, the ionization energy must be considered which reflects the difficulty of atomic losing electrons. Although Mn is oxygenophilic, it is hard for Mn to lose electrons, and the addition of Mn inhibits the electron transfer of Cr. The interaction between Mn and Cr may restrain the activity of Cr, leading to a weakening of the electron-losing capacity which is averse to electron transfer during OER performance.

Furthermore, the EXAFS characterization was conducted to disclose the coordination environment and the elements' oxidation states in the local structures of HEA NPs.[7,42–43] The FT-EXAFS spectra of Figure 5f indicate that metal–metal bonds of all FeCoNiCrN elements are slightly shifted, and the shortest neighbor atom distance for Cr implied that the electrons of Cr are more easily attracted to N, which is also consistent with the XPS analysis. The corresponding K-space data are also given in Figure S14a (Supporting Information), indicating the validity of R-space data. It is further evidence of a synergistic electronic coupling effect among the Fe, Co, Ni, Cr, and N atoms which may change the adsorption for the OER intermediates. What's more, the FT-EXAFS spectra (Figure S14b, Supporting Information) shows that the peaks of FeCoNiCrN and FeCoNiCr NPs with reduced intensity and their average bond length of Co were quite different from the metallic bond in foil Co reference, suggesting that the Co

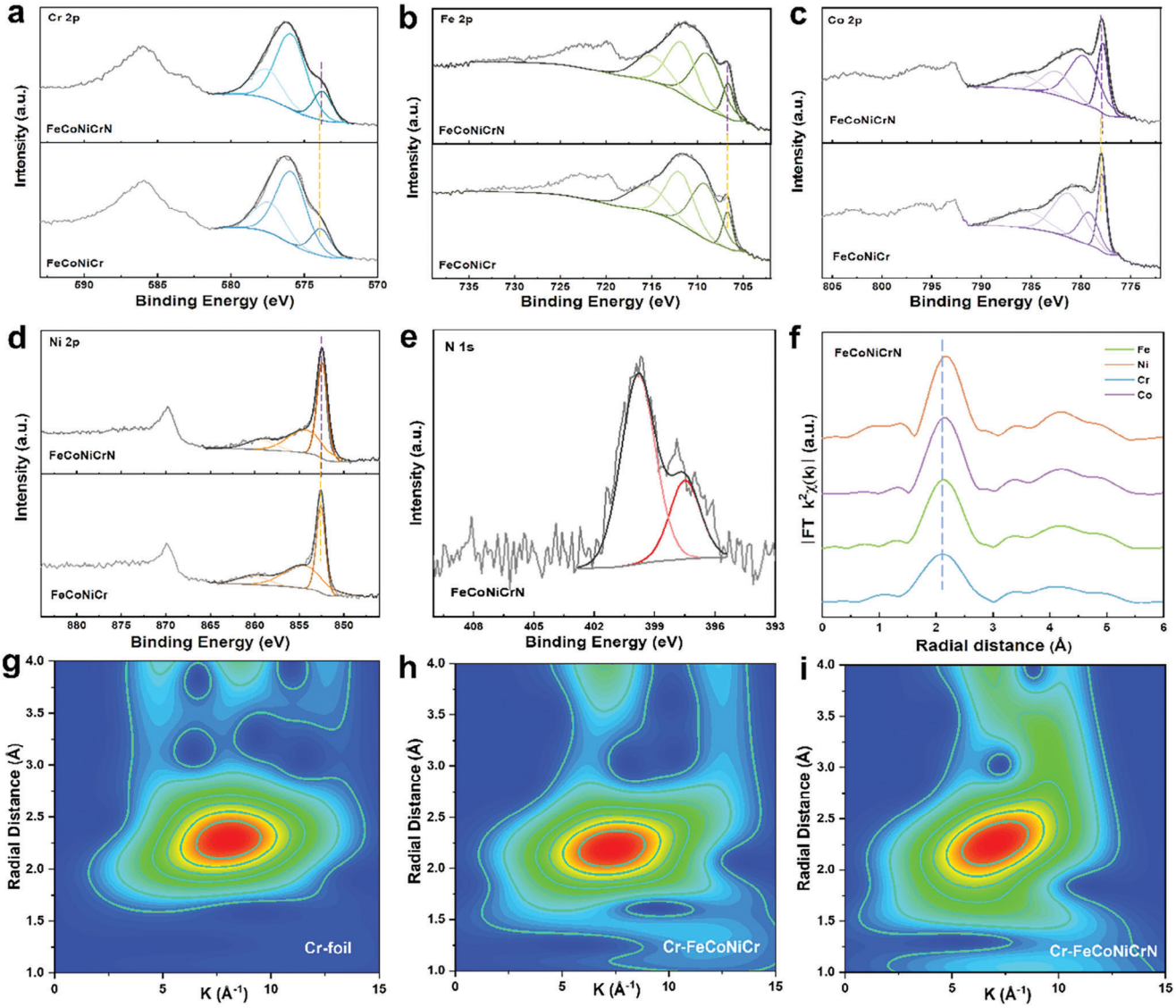

Figure 5. High-resolution XPS spectra of a) Cr 2p, b) Fe 2p, c) Co 2p, d) Ni 2p of FeCoNiCrN NPs and FeCoNiCr NPs; e) N 1s of FeCoNiCrN NPs; f) FT-EXAFS spectra of Fe, Co, Ni and Cr *K*-edge for FeCoNiCrN NPs; g—i) Wavelet transform plots for the Cr K-edge k^3-weighted EXAFS for foil, FeCoNiCr and FeCoNiCrN.

elements are surrounded by different metallic species (Fe, Cr, and Ni) and the generation of lattice distortion effects of HEA NPs. The peak shift of FeCoNiCrN toward lower radial distance could be attributed to N-doped. The local electronic structures of HEA NPs often relate to the underlying mechanism of the catalytic activity. A similar phenomenon can be more obviously seen in Figure 5g–i, the wavelet transform of Cr K-edge EXAFS further demonstrates the coordination environment of Cr in an intuitive way and Cr had a strong tendency to bond with N.[44]

It is essential to analyze the surface electrochemical states of FeCoNiCrN NPs. Hence, the valence changes of the catalysts in different state (the pristine, activated and CP-10 h of FeCoNiCrN NPs ink) are compared by XPS analysis. As displayed in **Figure 6**a, the binding energy peaks locate at 778.4, 781.4, 783.5, and 787.2 eV are contributed by Co^0, Co^{3+}, Co^{2+} and satellite peak, respectively. For Fe 2p, the multi-peak spectrum can be deconvoluted to reveal a composition of Fe^0, Fe^{2+}, Fe^{3+} and satellite peak, with the peaks of 707.5, 711.0, 713.1, and 715.0 eV, respectively. The Ni 2p spectrum are observed that the peaks at 853.3, 855.7, 857.3, and 861.6 eV correspond to Ni^0, Ni^{2+}, $Ni^{3+}$and satellite peak.[45] The binding energies of Cr^0, Cr^{3+} and Cr^{6+} were at 574.9, 576.6, and 578.8 eV, respectively. The intensity of the zero-valence peaks representing metals in FeCoNiCrN weaken significantly while that of the high valence states peaks strengthen after activation, indicating the transformation from M^0 to M^{2+}/M^{3+} possibly as well as the production of active intermediates including M-O/M-OH/M-OOH. Transition metallic elements with high valence states generally display superior catalytic activity. The increased electron holes in d-band of oxidized metal species with high valence can shift O 2p to the Fermi energy level as well as enhance the covalency of M-O bonds to boost the charge transfer.[46–48] As for the XPS fine spectrum of O 1s (Figure 6f),

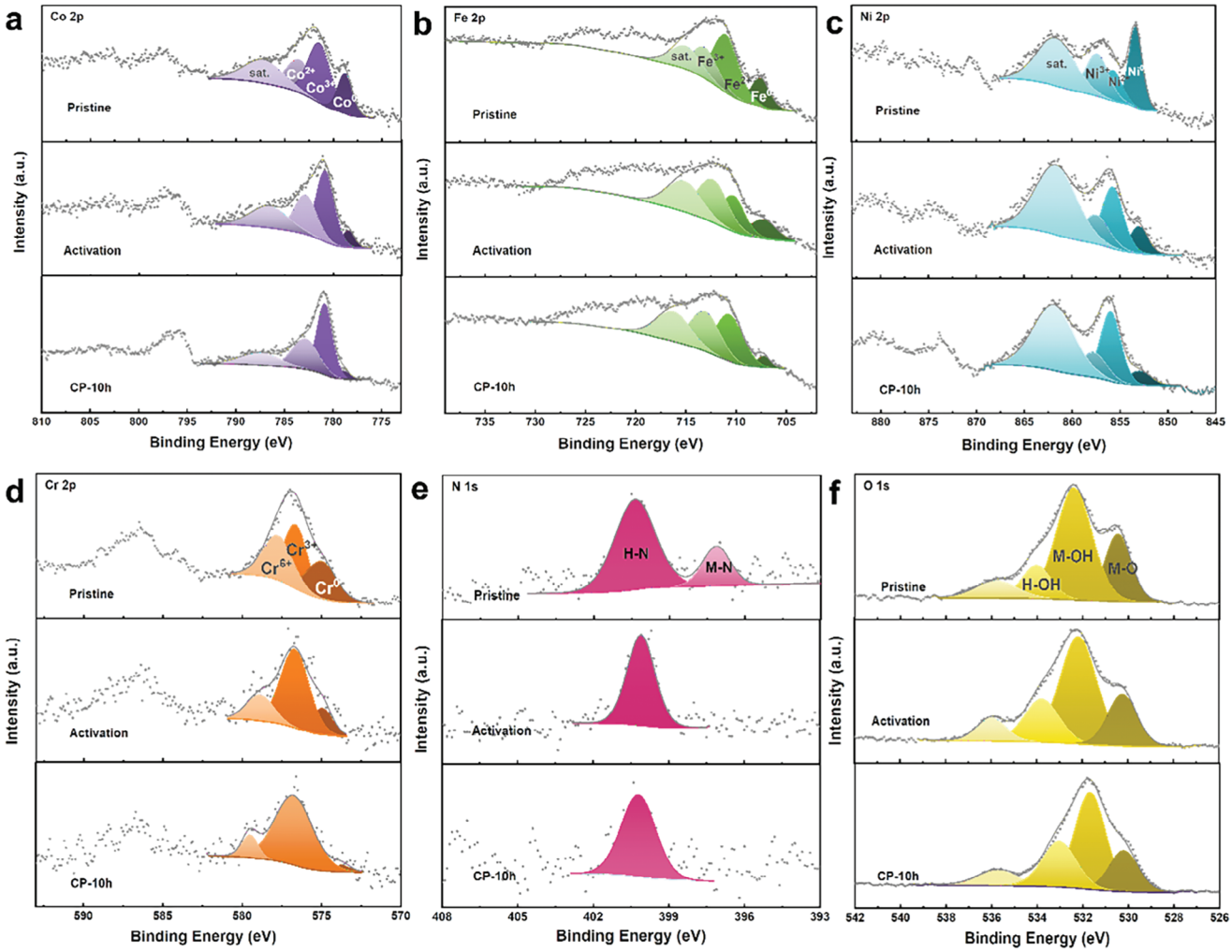

Figure 6. High-resolution XPS spectra of a) Co 2p, b) Fe 2p, c) Ni 2p, d) Cr 2p, e) N 1s, and f) O 1s of pristine, activation and CP-10 h FeCoNiCrN inks.

the peaks associate with the lattice oxygen bond (M−O), hydroxide bond (OH^-) and absorbed H_2O are located at 530.2, 531.9, and 533.1 eV,[49] respectively, which also correspond to the above results of the high valence metals generation. In general, the higher valence state can cause a downward shift of the metal d-band to overlap with the p-band of the oxygen ligand, diminishing the energy-limiting barrier to accelerate the OER kinetics. Meanwhile, to gain further insights on the stability behavior of FeCoNiCrN at OER, the surface chemical states are analyzed after 10 h of CP test via XPS. The intensity of metal zero-valence peaks is drastically reduced as compared with that of the sample before the CP-10 h test, indicating that the surface of FeCoNiCrN NPs had been irreversibly converted to (oxy)hydroxide-based compounds, while that of high valence metals peaks has been maintained at a high level which was the reason for the excellent stability of FeCoNiCrN NPs. The comparison of XPS spectrum between pristine-FeCoNiCrN and CP-10h-FeCoNiCrN in Figure S15 (Supporting Information), the relative content of oxygen significantly increased, corresponding to the production of (oxy)hydroxide-based compounds. The pronounced peak appeared at 397.1 eV is attributed to the M-N which faded away after stability testing, indicating the presence of partial N atom leaching.[50] This phenomenon also corresponds well to the EDS results, which the relative content of N decreased compared to before stability testing (1.63 at. % to 0.79 at. %). The leaching of N atoms under basic OER conditions may cause a certain surface reorganization of HEA NPs thus their electronic structure,[51] including the generation of defective sites, disorder, uncoordinated bonds, and potentially higher surface area which increases the active sites and thus affecting the stability. Additionally, Figure S16 (Supporting Information) shows the comparison among the pristine, activation and CP-10 h of FeCoNiCrN NPs by FTIR analysis. The broad absorption peak at 3556 cm^{-1} is the stretching vibration of hydroxyl (O-H) which is attributed to the generation of (oxy)hydroxide-Metals, and the -NH_2 stretching vibration is at 1608 cm^{-1} corresponding to the XPS results of N 1s spectrum.

3. Conclusion

To sum up, N-doped HEA NPs were designed and successfully synthesized via a unique green-nanofabrication IGC system. Multiple metallic elements combined uniformly is

benefited from the ultrarapid laser etching and cooling processes. N doping in HEA NPs can effectively enhance the flexibility in their electronic structures. The optimized FeCoNiCrN NPs exhibit an outstanding OER performance with an overpotential of 269.7 mV at a current density of 10 mA cm^{-2} and superior electrochemical stability. The FeCoNiCrMn//FeCoNiCrN couple delivers a current density of 10 mA cm^{-2} in 1.0 M KOH solution at 1.735 V for overall water splitting. In this work, the differences of electronegativity, ionization energy and electron affinity energy among mixed elements in N-doped HEAs were discussed as inducing electron transfer efficiency to create highly active sites with optimized energy barriers, which provides an in-depth understanding about the triggers of rapid electron transfer.

4. Experimental Section

Materials and Methods: Alloy ingots, as precursors, were obtained by typical arc-melting of mixtures consisting purity metal (≈99.9%) elements under a high-purity Ar atmosphere. A unique instrument for nanostructure preparation, i.e., IGC, was designed to evaporate via laser beam and simultaneously condense the evaporation products through liquid nitrogen under an inert gas atmosphere. The HEA NPs were manufactured from the above ingots via the IGC system. The scheme of preparation was illustrated in Figure 1a–c, where the HEA ingot as the target evaporated by laser beam, and then the evaporated HEA atoms condensed in He atmosphere as small crystals and accumulated on a copper roller filled with liquid nitrogen to form a loose powder that was subsequently collected by a scraper. A fast-cooling rate can suppress the precipitation of the second phase to form the solid-solution. Specially, the N-doped HEA NPs were prepared by a similar method under a N_2 atmosphere. All the samples were preserved in an oxygen-free environment.

Characterizations: Transmission electron microscopy (TEM), high-resolution transmission electron microscope (HRTEM) and energy dispersive spectroscopy (EDS) measurements were carried out by an FEI Talos F200S electron microscope operated at 200 kV. All TEM samples were prepared by depositing a drop of diluted ethanol suspension on a copper grid coated with a carbon film. X-ray photoelectron spectroscopy (XPS) data were recorded on a ULVCA-PHI spectrometer, and the spectra were calibrated reference to the C 1s peak (284.8 eV) as an internal standard. The crystal structures of the IGC-prepared HEA NPs were detected by synchrotron high-energy X-ray diffraction (XRD) at beamline 11-ID-C at the Advanced Photon Source, Argonne National Laboratory. High-energy monochromatic X-rays with a beam size of 500 μm × 500 μm and a wavelength of 0.1173 Å were used in transmission geometry for data collection. All the samples for synchrotron XRD measurements were sealed with Kapton tape. Extended X-ray absorption fine structure (EXAFS) of Fe, Co, Ni, Cr, and Mn K-edge were performed at Beamline 20-BM-B of Argonne National Laboratory to explore the electronic structures of catalysts. The FT-IR spectrum was recorded on a Bruker TENSOR27 FTIR spectrometric analyzer with KBr pellets.

Electrochemical Measurements: The electrochemical performance was assessed on an electrochemical workstation (CHI660E, Shanghai Chen Hua Ltd., China) via the traditional three-electrode cell at 25 °C in 1 M potassium hydroxide (KOH) electrolyte. The catalyst-modified glassy carbon (GC) was used as the working electrode, as well as the Pt sheet and Hg/HgO electrode were used as the counter electrode and the reference electrode, respectively. Nevertheless, the counter electrode was graphite sheet in the HER reaction due to the sensitivity of the Pt. The catalyst ink contained the as-synthesized catalysts (6 mg), conductive carbon (4 mg) and 5 wt. % Nafion (20 μL) were ultrasonically dispersed in 980 mL of the absolute ethanol for 60 min to obtain a homogenous suspension. In total 10-μL of the homogeneous dispersion was transferred onto the surface of the GC substrate (0.19625 cm^2) twice and dried at room temperature. The catalyst mass loading was ≈0.306 mg cm^{-2}. The electrolyte was purged with O_2 (for OER) or N_2 (for HER) for 30 min before each test, and then the working electrode was activated by Cyclic voltammograms (CVs) tests. All the potentials reported were referenced versus reversible hydrogen electrode (RHE) with IR compensation. Linear sweep voltammetry (LSV) test, as an essential indicator, was carried out evaluating electrocatalytic performance and the scanning rate was 5 mV s^{-1}. CVs tests were performed in the potential window of 0.92 – 1.02 V (versus Hg/HgO) with different sweeping rates from 10 to 100 mV s^{-1} to calculate the electrochemical double-layer capacitances (Cdl). Electrochemical impedance spectroscopy (EIS) measurements were performed in the frequency range of 10^5 Hz to 0.01 Hz at 0.6 V versus Hg/HgO for OER and −1.25 V versus Hg/HgO for HER, respectively. Durability was evaluated by chronopotentiometry test under a constant current density of 10 mA cm^{-2}. In order to calculate ECSA, the applied specific capacitance (20—60 μF cm^{-2}) was set as 40 μF cm^{-2}.[46]

$$ECSA = Cdl/Cs \times ASA \quad (1)$$

where Cs was the specific capacitance and ASA was the actual surface area of substrates. The Chronopotentiometry (CP) test or Amperometric i-t Curve (i-t) was executed to detect the stability of the catalysts.[52] Inevitably, due to the weak mechanical bonding and the violent production of gas bubbles during HER/OER test at high current density, the catalyst film as the working electrode can fall off on the surface of the glass-carbon electrode. Therefore, carbon cloth was selected as a support for the durability test of 1000 times CV and CP measurement at 100 mA cm^{-2} for HER/OER test.

Acknowledgements

This work was financially supported by the National Key R&D Program of China (no. 2021YFB3802800), the National Natural Science Founda-tion of China (nos. 12261160364, 52101195, 52222104), the Fundamen-tal Research Funds for the Central Universities (nos. 30919011404 and 30919011107). This research also used resources of the Advanced Photon Source, a U.S. Department of Energy (DOE) Office of Science User Facility operated for the DOE Office of Science by Argonne National Laboratory under Contract No. DE-AC02-06CH11357.

Conflict of Interest

The authors declare no conflict of interest.

Data Availability Statement

The data that support the findings of this study are available from the corresponding author upon reasonable request.

Keywords

electron transfer, high-entropy alloy, inert gas condensation, nanocrystalline, nitrogen doping, oxygen evolution reaction, water splitting

[1] Y. Zhang, D. Wang, S. Wang, *Small* **2022**, *18*, e2104339.
[2] Y. Wang, Y. Wang, *Nano Energy* **2022**, *104*, 107958.
[3] Y. Sun, S. Dai, *Sci. Adv.* **2021**, *7*, eabg1600.
[4] R. Jiang, Y. Da, X. Han, Y. Chen, Y. Deng, W. Hu, *Cell Rep. Phys. Sci.* **2021**, *2*, 100302.
[5] J. Wang, S. Wu, S. Fu, S. Liu, Z. Ren, M. Yan, S. Chen, S. Lan, H. Hahn, T. Feng, *J. Mater. Sci. Technol.* **2021**, *77*, 126.
[6] S. Wu, Z. Kou, J. Wang, M. Yan, S. Fu, S. Lan, Q. Lai, T. Feng, *Mater. Charact.* **2021**, *178*, 111238.
[7] H. Wu, Q. Lu, Y. Li, J. Wang, Y. Li, R. Jiang, J. Zhang, X. Zheng, X. Han, N. Zhao, J. Li, Y. Deng, W. Hu, *Nano Lett.* **2022**, *22*, 6492.
[8] S. Gao, S. Hao, Z. Huang, Y. Yuan, S. Han, L. Lei, X. Zhang, R. Shahbazian-Yassar, J. Lu, *Nat. Commun.* **2016**, *2020*, 11.
[9] Z. W. Seh, J. Kibsgaard, C. F. Dickens, I. Chorkendorff, J. K. Nørskov, T. F. Jaramillo, *Science* **2017**, *355*, aad4998.
[10] S. Zhang, J. Guo, T. Li, J. Sun, Y. Meng, J. Kang, L. Tan, Z. Zhang, *Appl. Surf. Sci.* **2023**, *608*, 155221.
[11] J. You, R. Yao, W. Ji, Y. Zhao, Z. Wang, *J. Alloys Compd.* **2022**, *908*, 164669.
[12] Q. Jiang, R. Lu, J. Gu, L. Zhang, K. Liu, M. Huang, P. Liu, S. Zuo, Y. Wang, Y. Zhao, P. Ma, Z. Fu, *Chem. Eng. J.* **2023**, *453*, 139510.
[13] Z. Xue, X. Zhang, J. Qin, R. Liu, *J. Energy Chem.* **2021**, *55*, 437.
[14] K. Zhang, R. Zou, *Small* **2021**, *17*, e2100129.
[15] X. Wang, Z. Pan, X. Chu, K. Huang, Y. Cong, R. Cao, R. Sarangi, L. Li, G. Li, S. Feng, *Angew. Chem. Int. Ed. Engl.* **2019**, *58*, 11720.
[16] Y. Ma, Y. Ma, Q. Wang, S. Schweidler, M. Botros, T. Fu, H. Hahn, T. Brezesinski, B. Breitung, *Energy Environ. Sci.* **2021**, *14*, 2883.
[17] T. Yu, H. Xu, Z. Jin, Y. Zhang, H.-J. Qiu, *Appl. Surf. Sci.* **2023**, *610*, 155624.
[18] L. Li, H. Yang, J. Miao, L. Zhang, H.-Y. Wang, Z. Zeng, W. Huang, X. Dong, B. Liu, *ACS Energy Lett.* **2017**, *2*, 294.
[19] J. Yan, M. Tian, R. Shi, T. Gu, K. Zeng, J. Zhou, Q. Zhang, M. H. Rümmeli, R. Yang, *Mater. Today Energy* **2022**, *30*, 101171.
[20] F. Li, Y. Ma, H. Wu, Q. Zhai, J. Zhao, H. Ji, S. Tang, X. Meng, *J. Phys. Chem. C* **2022**, *126*, 18323.
[21] W.-F. Chen, K. Sasaki, C. Ma, A. I. Frenkel, N. Marinkovic, J. T. Muckerman, Y. Zhu, R. R. Adzic, *Angew. Chem. Int. Ed. Engl.* **2012**, *51*, 6131.
[22] L. Pu, J. Zhang, N. K. L. Jiresse, Y. Gao, H. Zhou, N. Naik, P. Gao, Z. Guo, *Adv. Compos. Hybrid Mater.* **2021**, *5*, 356.
[23] T.-Y. Su, G.-P. Lu, K.-K. Sun, M. Zhang, C. Cai, *Catal. Sci. Technol.* **2022**, *12*, 2106.
[24] X. Peng, C. Pi, X. Zhang, S. Li, K. Huo, P. K. Chu, *Sustainable Energy Fuels* **2019**, *3*, 366.
[25] M. Luo, S. Guo, *Nat. Rev. Mater.* **2017**, *2*, 17059.
[26] Z. Lei, X. Liu, Y. Wu, H. Wang, S. Jiang, S. Wang, X. Hui, Y. Wu, B. Gault, P. Kontis, D. Raabe, L. Gu, Q. Zhang, H. Chen, H. Wang, J. Liu, K. An, Q. Zeng, T.-G. Nieh, Z. Lu, *Nature* **2018**, *563*, 546.
[27] M. Song, R. Zhou, J. Gu, Z. Wang, S. Ni, Y. Liu, *Appl. Mater. Today* **2020**, *18*, 100498.
[28] Y. Xiong, Y. Ma, L. Zou, S. Han, H. Chen, S. Wang, M. Gu, Y. Shen, L. Zhang, Z. Xia, J. Li, H. Yang, *J. Catal.* **2020**, *382*, 247.
[29] F. Waag, Y. Li, A. R. Ziefuß, E. Bertin, M. Kamp, V. Duppel, G. Marzun, L. Kienle, S. Barcikowski, B. Gökce, *RSC Adv.* **2019**, *9*, 18547.
[30] O. Auciello, A. V. Sumant, *Diamond Relat. Mater.* **2010**, *19*, 699.
[31] S.-C. Liang, D.-C. Tsai, Z.-C. Chang, H.-S. Sung, Y.-C. Lin, Y.-J. Yeh, M.-J. Deng, F.-S. Shieu, *Appl. Surf. Sci.* **2011**, *258*, 399.
[32] Y. Chen, X. Zhan, S. L. A. Bueno, I. H. Shafei, H. M. Ashberry, K. Chatterjee, L. Xu, Y. Tang, S. E. Skrabalak, *Nanoscale Horiz.* **2021**, *6*, 231.
[33] S.-Q. Chang, C.-C. Cheng, P.-Y. Cheng, C.-L. Huang, S.-Y. Lu, *Chem. Eng. J.* **2022**, *446*, 137452.
[34] M. Han, C. Wang, J. Zhong, J. Han, N. Wang, A. Seifitokaldani, Y. Yu, Y. Liu, X. Sun, A. Vomiero, H. Liang, *Appl. Catal., B* **2022**, *301*, 120764.
[35] C. Spöri, P. Briois, H. N. Nong, T. Reier, A. Billard, S. Kühl, D. Teschner, P. Strasser, *ACS Catal.* **2019**, *9*, 6653.
[36] S. Wang, W. Huo, F. Fang, Z. Xie, J. K. Shang, J. Jiang, *Chem. Eng. J.* **2022**, *429*, 132410.
[37] J. Hao, Z. Zhuang, K. Cao, G. Gao, C. Wang, F. Lai, S. Lu, P. Ma, W. Dong, T. Liu, M. Du, H. Zhu, *Nat. Commun.* **2022**, *13*, 2662.
[38] T. Wang, H. Chen, Z. Yang, J. Liang, S. Dai, *J. Am. Chem. Soc.* **2020**, *142*, 4550.
[39] X. Chen, N. Li, Z. Kong, W.-J. Ong, X. Zhao, *Mater. Horiz.* **2018**, *5*, 9.
[40] H. Chen, X. Liang, Y. Liu, X. Ai, T. Asefa, X. Zou, *Adv. Mater.* **2020**, *32*, 2002435.
[41] N. Govindarajan, M. T. M. Koper, E. J. Meijer, F. Calle-Vallejo, *ACS Catal.* **2019**, *9*, 4218.
[42] J. Ding, D. Wu, J. Zhu, S. Huang, F. Rodríguez-Hernández, Y. Chen, C. Lu, S. Zhou, J. Zhang, D. Tranca, X. Zhuang, *Chem. Eng. J.* **2021**, *426*, 131320.
[43] J. X. Yang, B.-H. Dai, C.-Y. Chiang, I.-C. Chiu, C.-W. Pao, S.-Y. Lu, I.-Y. Tsao, S.-T. Lin, C.-T. Chiu, J.-W. Yeh, P.-C. Chang, W.-H. Hung, *ACS Nano* **2021**, *15*, 12324.
[44] F. Lyu, S. Zeng, Z. Jia, F.-X. Ma, L. Sun, L. Cheng, J. Pan, Y. Bao, Z. Mao, Y. Bu, Y. Y. Li, J. Lu, *Nat. Commun.* **2022**, *13*, 6249.
[45] P. A. Sukkurji, Y. Cui, S. Lee, K. Wang, R. Azmi, A. Sarkar, S. Indris, S. S. Bhattacharya, R. Kruk, H. Hahn, Q. Wang, M. Botros, B. Breitung, *J. Mater. Chem. A* **2021**, *9*, 8998.
[46] N. Zhang, X. Feng, D. Rao, X. Deng, L. Cai, B. Qiu, R. Long, Y. Xiong, Y. Lu, Y. Chai, *Nat. Commun.* **2020**, *11*, 4066.
[47] J. Suntivich, K. J. May, H. A. Gasteiger, J. B. Goodenough, Y. Shao-Horn, *Science* **2011**, *334*, 1383.
[48] A. Grimaud, A. Demortière, M. Saubanère, W. Dachraoui, M. Duchamp, M.-L. Doublet, J.-M. Tarascon, *Nat. Energy* **2016**, *2*, 16189.
[49] J. Xia, H. Zhao, B. Huang, L. Xu, M. Luo, J. Wang, F. Luo, Y. Du, C.-H. Yan, *Adv. Funct. Mater.* **2020**, *30*, 1908367.
[50] Q. Du, P. Su, Z. Cao, J. Yang, C. A. H. Price, J. Liu, *Sustain. Mater. Technol.* **2021**, *29*, e00293.
[51] X. Wang, Y. Zuo, S. Horta, R. He, L. Yang, A. Ostovari Moghaddam, M. IbEz, X. Qi, A. Cabot, *ACS Appl. Mater. Interfaces* **2022**, *14*, 48212.
[52] Q. Wen, Y. Zhao, Y. Liu, H. Li, T. Zhai, *Small* **2022**, *18*, e2104513.